CHAPTER III

RADIATIVE FORCING

This chapter describes the optical properties of the Pinatubo aerosol and the radiative forcing by the Pinatubo aerosol from June 1991 through May 1993. The radiative–transfer model (RTM) of the UIUC 24–layer stratosphere/troposphere general circulation model (ST–GCM) is used for the forcing calculation.

A. Introduction

The estimate of the radiative forcing by the Pinatubo volcanic aerosol serves two purposes. First, it is for the reconstruction of the radiative forcing of historical volcanic eruptions (Andronova *et al.* 1999). This reconstruction has been used to investigate the climate sensitivity and the observed climate changes in the past century (Andronova and Schlesinger 2000). Second, it serves as input for climate models to simulate the climate changes induced by the Pinatubo volcanic aerosol.

Atmospheric general circulation models (AGCM) have been used in a few studies to understand the climatic impact of the Pinatubo eruption (Hansen *et al.* 1992, 1996; Kirchner and Graf 1995; Kirchner *et al.* 1999). An accurate description of the optical properties of the volcanic aerosol in time and space is vital for the AGCMs to calculate correctly the radiative forcing and to simulate the responses of the climate to the forcing. Though the Pinatubo eruption has been the best observed in history by satellites and ground–based observation stations, the observed database on its own is still not adequate enough for global studies. To accurately calculate the aerosol optical properties needs detailed measurements of the spatial and temporal distributions of aerosol mass, size distribution, chemical composition and/or refractive index following the eruption. However, such a dataset does not exist. Ground–based observations and aircraft, balloon, and spacecraft observations were confined to specific locations and times. Some technique limitations constrained the desired usage of satellite observations (Russell *et al.* 1996). SAGE–II, a limb–occultation instrument, measures the intensity of the direct solar beam before and after the solar beam is attenuated. It measures aerosol extinction at four wavelengths (0.38, 0.45, 0.525, and 1.02 μm)

with a fine vertical resolution of approximate 1 km, and is self–calibrating and highly sensitive to small optical depth. However, its temporal and horizontal resolutions are coarse. No data were available at the time and latitude of the greatest optical depth following the eruption (August–September, 1991; 5°N ~ 20°S) because at wavelength 0.525 μm, optical depths larger than about 0.2 become saturated. On the other hand, AVHRR has a fine horizontal (~1.1 km) and temporal (about one week) resolution and is able to detect aerosol optical depth up to about 2, above which aerosols and clouds cannot be distinguished from each other. However, it has no vertical resolution. The product is available at only one wavelength (0.5 μm). To derive optical depth from the measured radiance requires pre–existing knowledge of the size distribution and refractive index of aerosol particles. Consequently, the optical depth at 0.5 μm derived from AVHRR differs greatly from that at 0.525 μm observed by SAGE–II in the tropics, where dense aerosol clouds existed (Andronova *et al.* 1999).

Due to the lack of a self–consistent dataset of aerosol optical properties for the Pinatubo volcanic eruption, Hansen *et al.* (1992) and Kirchner and Graf (1995) had to use highly simplified datasets created based on the limited measurements of El Chichón eruption and certain then–available information about the Pinatubo eruption to simulate the potential climatic impact of the Pinatubo eruption. In recent years, a few studies have attempted to reconstruct a consistent dataset of aerosol optical properties for the Pinatubo eruption. For example, Russell *et al.* (1996) assembled the data on the Pinatubo volcanic aerosol from space, air and ground measurements and developed a composite dataset along with estimates of the uncertainties of measurement and retrieval techniques. Stenchikov *et al.* (1998) (hereinafter referred to as ST98) developed a time–dependent, zonally averaged, vertically resolved spectral dataset of the Pinatubo aerosol optical properties covering the time from June 1991 through May 1993. They used data derived from SAGE–II, UARS, balloon, and lidar observations together with a Mie scattering model and the ECHAM4 GCM. This dataset has been used to compute the radiative forcing of the Pinatubo eruption by ST98, and to simulate the climate changes induced by the forcing by running the ECHAM4 GCM (Kirchner *et al.* 1999).

Collaborating with Dr. Stenchikov, we reconstructed a new dataset of the Pinatubo aerosol optical properties using the techniques of ST98, but based on the radiation spectral bands and spatial

structure of the UIUC 24–layer ST–GCM. Section B describes the reconstruction method and the reconstructed dataset of aerosol optical properties. Results are compared with satellite observations and ST98's calculation. Section C presents the calculated radiative forcing during the two years following the eruption.

B. Aerosol Optical Properties

To calculate the radiative forcing by the Pinatubo aerosol using the RTM of the UIUC 24–layer ST–GCM requires the time and spatially varying broad–band–averaged aerosol extinction, single–scattering albedo and asymmetry factor. We use the same approach and model package that ST98 used to derive the monthly zonal–mean aerosol optical properties. As described in ST98 the observed SAGE–II aerosol extinction for λ = 1.02 μm (McCormick *et al.* 1995) and the UARS–retrieved effective radius (Lambert *et al.* 1997) comprise the basis for the derivation, and the Mie theory code of Wiscombe (1980) was used to calculate the aerosol's spectral optical properties. For each month from June 1991 through May 1993, Mie calculations were performed for 60 selected spectral bands from 0.2 μm to 145 μm for the 24 vertical layers of each of the 3312 grid cells of the ST–GCM's 4^{o}–latitude by 5^{o}–longitude resolution. Then, the calculated aerosol optical properties were averaged for the 20 broad bands of the radiation modules of the 24–layer ST–GCM (see Appendix A Tables A–1 and A–2) by using the Planck functions at T = 6000K and T = 300K as weights for the solar and longwave bands, respectively. The Mie calculation used the refractive index for a 75% solution of sulfuric acid (Palmer and Williams 1975) and a unimodal lognormal aerosol size distribution. Iterative procedures were used to determine the best standard deviation of the size distribution to get a best fit of the calculated and UARS–retrieved optical depth at 12.66 μm. In short, this calculation differs from ST98 in: (1) all vertical interpolations were performed such that the total optical depth for 1.02 μm was conserved; and (2) for consistency, the derivation was performed for the spatial grid and spectral bands of the UIUC 24–layer ST–GCM. Both of these differences improve the calculation of the optical properties of the volcanic aerosol. The first difference is important because it correctly defines the total number of aerosol particles in the column

in the spectral band where the most representative observational data exist, and the second difference improves the vertical and spectral representation of the Pinatubo aerosol cloud. The atmospheric conditions that are required to derive the aerosol optical properties, such as the geopotential heights of isobaric surfaces, were obtained from the climatology simulated by the UIUC 24–layer ST–GCM (Appendix A).

Because of the differences between the calculations of the aerosol optical properties performed here and by ST98, we compare the optical depth calculated for the two models with each other and with observations. Fig. 3.1 presents the monthly mean zonally averaged column–integrated aerosol optical depths at $\lambda = 0.55$ μm and $\lambda = 1.02$ μm for the period June 1991 – May 1993 calculated for the UIUC 24–layer ST–GCM (Figs. 3.1a and 3.1e) and for the ECHAM4 GCM (ST98) (Figs. 3.1b and 3.1f), and as observed by SAGE–II at $\lambda = 0.525$ μm and $\lambda = 1.02$ μm (Figs. 3.1c and 3.1g) and by AVHRR at $\lambda = 0.55$ μm (Fig. 3.1d).

The optical depth at $\lambda = 0.55$ μm calculated for the UIUC ST–GCM (Fig. 3.1a) has a similar latitude–time distribution as the optical depth calculated for the ECHAM4 GCM (ST98) (Fig. 3.1b), but is generally larger, especially in the middle and high latitudes where our optical depth reaches 0.15 to 0.25 while the ST98 is only about 0.1. Also the calculations for the UIUC ST–GCM reveal a secondary optical–depth maximum in the high latitudes of both hemispheres, which is absent in ST98. Calculation of the column–integrated optical depth for $\lambda = 0.55$ μm for the UIUC ST–GCM agrees better with the AVHRR observation (Fig. 3.1d) than does the optical depth of ST98, even though both the calculated optical depths are smaller than the observed by AVHRR. As mentioned by Long and Stowe (1994), AVHRR might have overestimated the optical depth because of a deficiency of the retrieval algorithm. The discrepancy between the SAGE–II (Fig. 3.1c) and AVHRR data defines the level of uncertainty in observations.

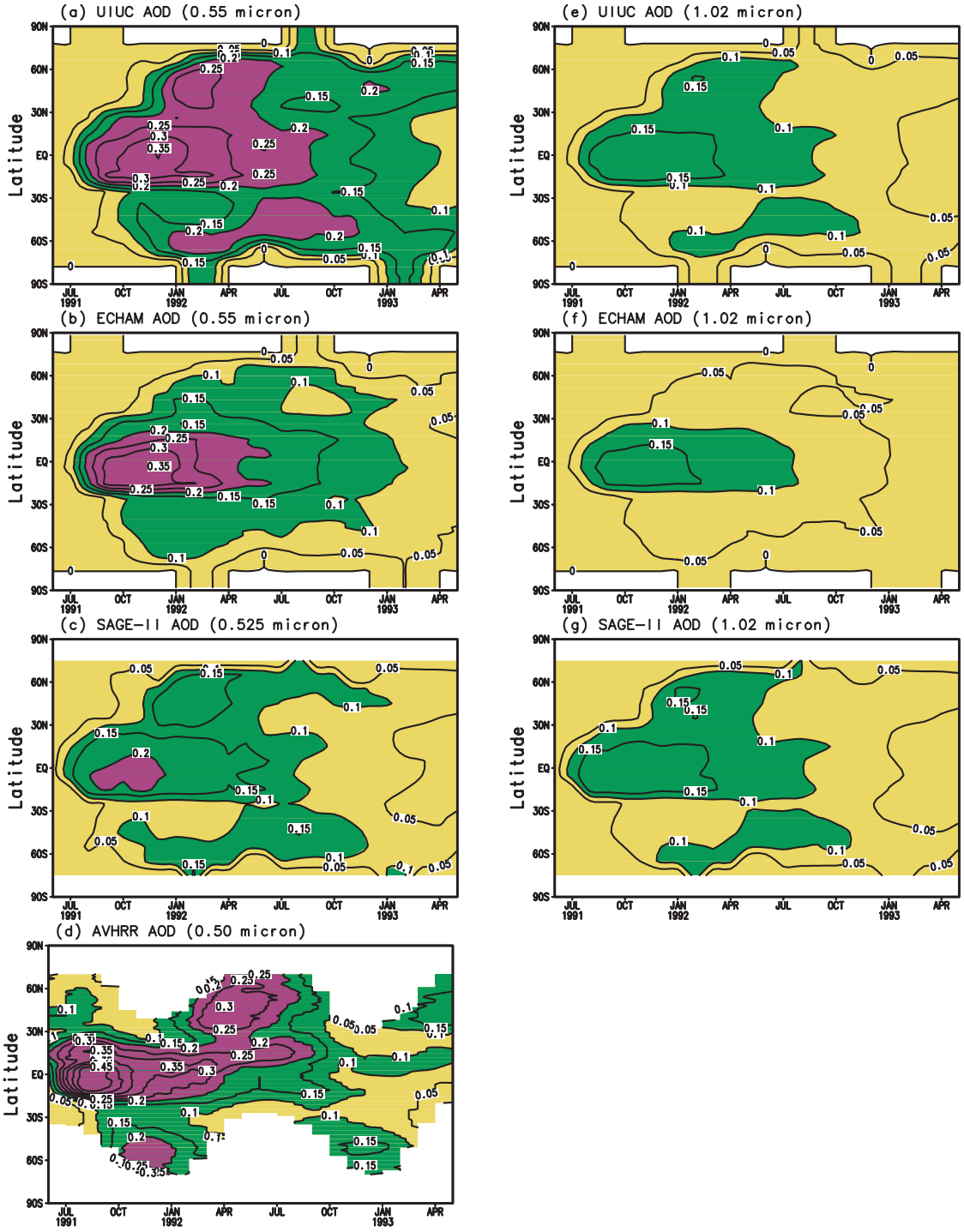

Fig. 3.1. *Zonally averaged column–integrated monthly mean aerosol optical depths at λ = 0.55 μm and λ = 1.02 μm for the period June 1991 – May 1993. (a) and (e): calculated for the UIUC 24–layer ST–GCM; (b) and (f): calculated for the ECHAM4 GCM by ST98; (c) and (g): observed by SAGE–II at λ = 0.525 μm and λ = 1.02 μm; (d): observed by AVHRR at λ = 0.50 μm.*

Comparison of Figs. 3.1e–g shows that, as expected, the calculation of the column–integrated optical depth at $\lambda = 1.02$ μm for the UIUC ST–GCM agrees exactly with the SAGE–II observation, while the ST98's calculation underestimated the optical depth, especially in the middle and high latitudes of both hemispheres. In general we explain the larger optical depths for both spectral intervals ($\lambda = 0.55$ μm and $\lambda = 1.02$ μm) obtained here for the UIUC ST–GCM than by ST98 for the ECHAM4 GCM as mostly due to our constraint on the calculation here of the optical depth at $\lambda = 1.02$ μm. Overall, the UIUC ST–GCM gives an improved representation of the optical properties of the Pinatubo aerosol.

We compare further the averaged total optical depths over the area covered by SAGE–II (Fig. 3.2a) and over the area covered by AVHRR (Fig. 3.2b). The wavelengths are 0.525 μm for SAGE–II, 0.50 μm for AVHRR, and 0.55 μm for both the UIUC ST–GCM and ECHAM4 GCM. We also included in Fig. 3.2 the optical depths at 0.55 μm compiled by Sato *et al.* (1993) for historical volcanic eruptions. The maximum total optical depths averaged over the SAGE–II covered area (75°S ~ 75°N) are 0.228 for the UIUC ST–GCM in February 1992, 0.186 for the ECHAM4 GCM in December 1991, 0.145 for SAGE–II in February 1992, and 0.150 for Sato *et al.* (1993) in February 1992. In Fig. 3.2b the maximum total optical depth for AVHRR at 0.5 μm occurred two to three months earlier and is much larger than that for SAGE–II at 0.525 μm. The discrepancies in timing and magnitude were caused by the differences in the techniques of measuring and retrieval between SAGE–II and AVHRR (Russell *et al.* 1996). Overall, the calculated total optical depth for the UIUC ST–GCM is generally larger than that for the ECHAM4 GCM. This is mostly due to our constraint on the calculation of the optical depth at $\lambda = 1.02$ μm for the UIUC ST–GCM. The calculated total optical depths for both the UIUC ST–GCM and the ECHAM4 GCM are mostly close to the SAGE–II observation in timing and to the AVHRR observation in magnitude.

We compared the reconstructed total optical depth at 0.55 μm with the observed at 0.525 μm for SAGE–II and 0.50 μm for AVHRR in Figs. 3.1 and 3.2. Are these comparisons valid? Does total optical depth depend on wavelength? Fig. 3.3 presents the total optical depths calculated for the UIUC ST–GCM and calculated by ST98 for the ECHAM4 GCM for the wavelengths from 0.2 μm

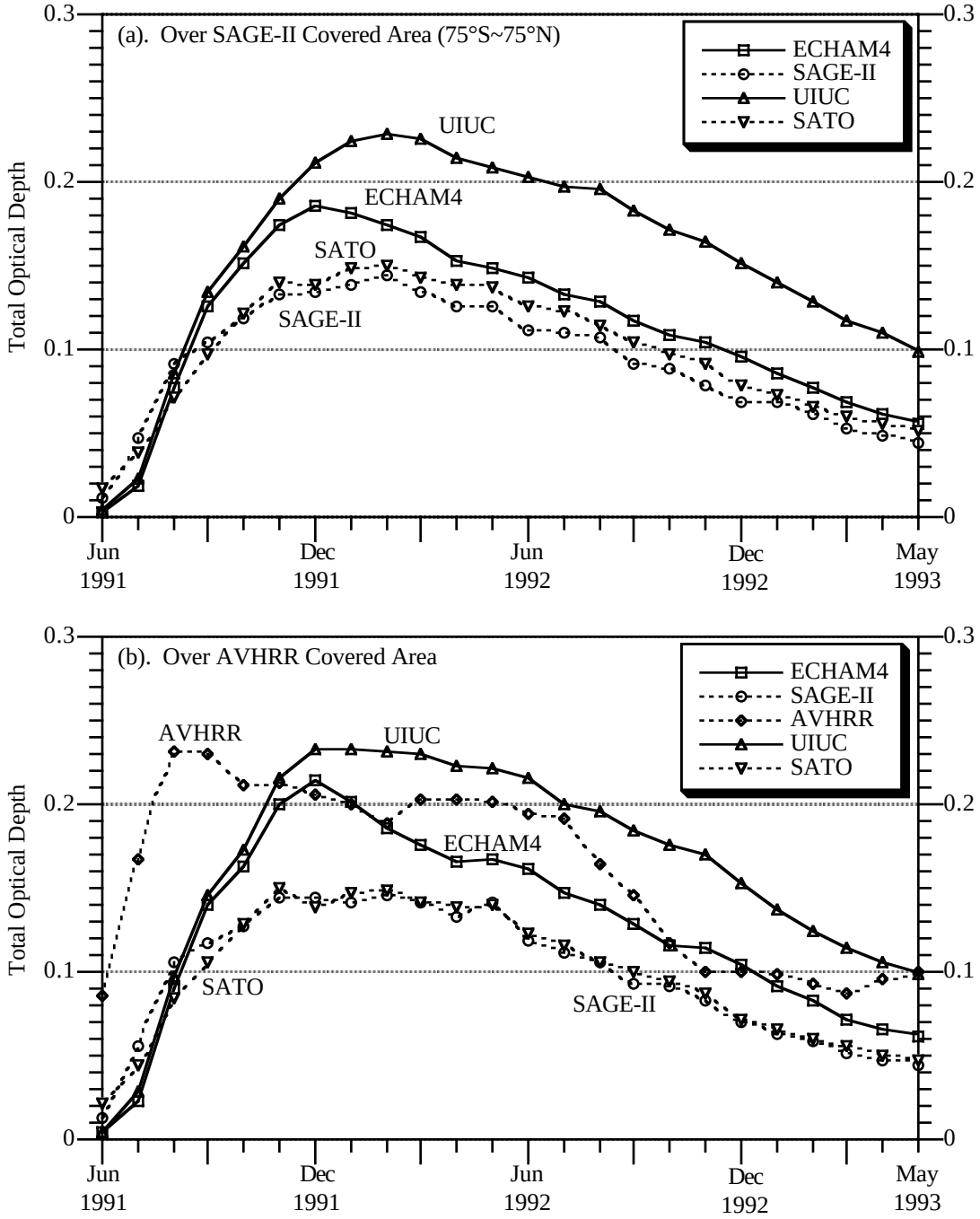

Fig. 3.2. *Averaged total optical depth (a) over the area covered by SAGE–II (see Fig. 3.1c) and (b) over the area covered by AVHRR (see Fig. 3.1d) for wavelengths at 0.525 μm for SAGE–II, 0.50 μm for AVHRR, and 0.55 μm for both the UIUC ST–GCM and ECHAM4 GCM.*

to 30 μm in January 1992 at the equator. For either calculation the total optical depth at 0.50 μm is very close to that at 0.55 μm. This should also be true for observations if either SAGE–II or AVHRR had operated at these two wavelengths simultaneously. Therefore, the comparisons in Figs. 3.1 and 3.2 should be qualitatively accurate. Fig. 3.3 also shows that the total optical depth strongly depends on wavelength. It reaches the maximum in the visible region and drops very fast in the near–infrared region. Even though the total optical depth at 0.55 μm shown in Figs. 3.1 and 3.2 for the UIUC ST–GCM is larger than that for the ECHAM4 GCM, the total optical depth at wavelengths smaller than 0.5 μm for the UIUC ST–GCM is smaller than that for the ECHAM4 GCM in Fig. 3.3.

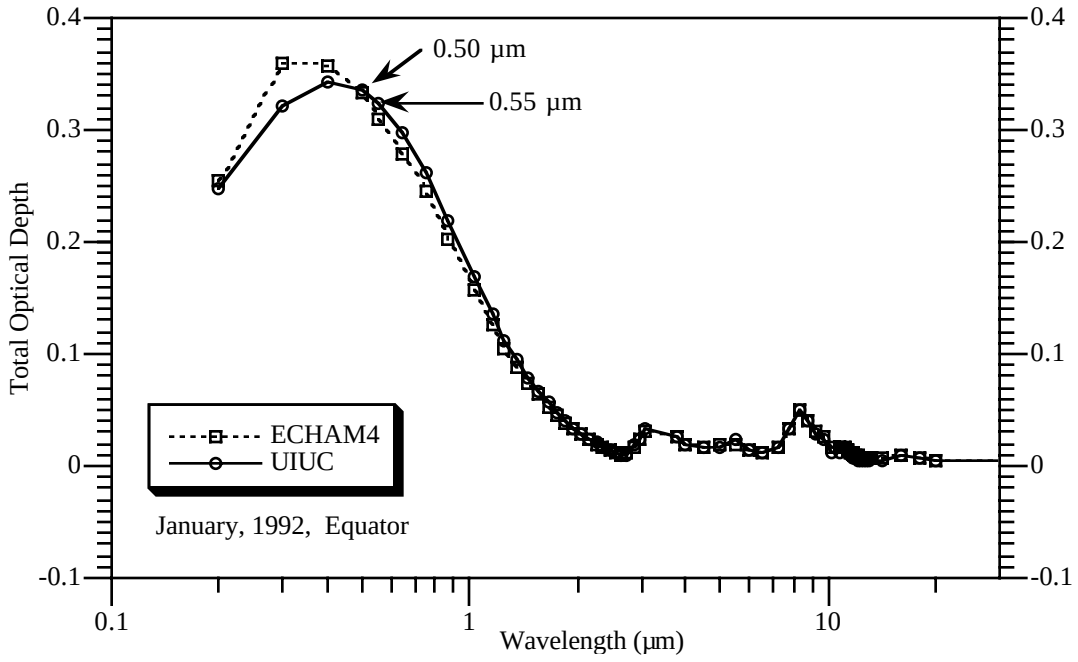

Fig. 3.3. *Total optical depth at the wavelengths from 0.2 μm to 30 μm in January 1992 at the equator calculated for the UIUC 24–layer ST–GCM and calculated by ST98 for the ECHAM4 GCM.*

Fig. 3.4 shows the time–altitude distributions of aerosol extinction (1/m) at the equator at $\lambda = 0.55$ μm calculated for the UIUC ST–GCM and calculated by ST98 for the ECHAM4 GCM. It

can be seen that a part of the Pinatubo aerosol cloud is located above 10 hPa. This high–altitude part of the aerosol cloud is better resolved by the UIUC ST–GCM than by the ECHAM4 GCM since the ECHAM4 GCM has only one layer between 20 hPa and 0 hPa. This is an advantage of the UIUC ST–GCM.

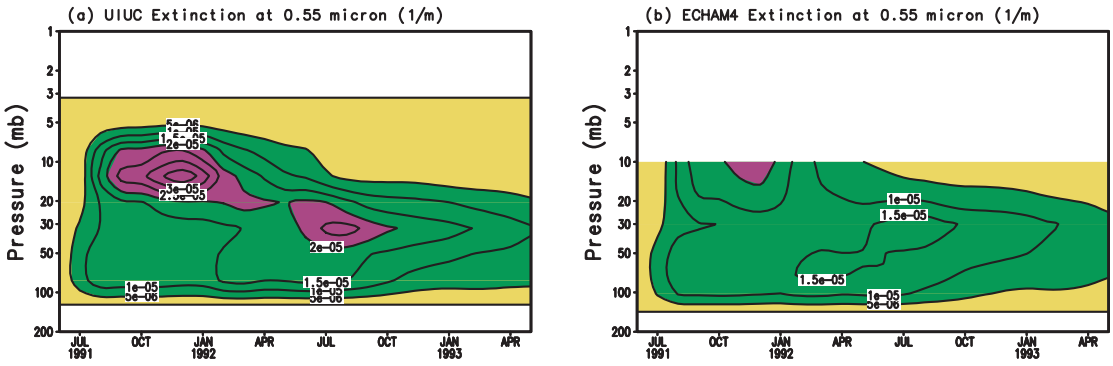

Fig. 3.4. *Vertical distributions of the specific extinction at λ = 0.55 µm at the equator for the period June 1991 – May 1993 calculated for (a) the UIUC 24–layer ST–GCM and (b) for the ECHAM4 GCM by ST98.*

C. Radiative Forcing

1. Definitions of Radiative Forcing

There are currently a few different definitions of radiative forcing in use. Basically radiative forcing is defined as the change in the net radiative flux at a given level of the atmosphere induced by an external perturbation to the atmosphere. The level can be the top of the atmosphere, the tropopause, or the earth's surface. The calculation can be performed without the response of the atmosphere to the perturbation, the so–called instantaneous forcing, or with the responses of the whole or part of the atmosphere to the perturbation, the so–called adjusted forcing. For example, the Intergovernmental Panel on Climate Change (IPCC) 1994 report (Houghton *et al.* 1995) defined radiative forcing as the change in the net radiative flux at the tropopause after the stratosphere has reached radiative equilibrium, but without the tropospheric responses. ST98 defined the radiative

forcing of volcanic aerosol as the change in the net radiative flux at the earth's surface and the change in atmospheric heating rate either with or without the response of the whole atmosphere to the perturbation.

The forcing defined at the tropopause with stratospheric adjustment by the IPCC 1994 report (Houghton *et al.* 1995) treats the response of the stratospheric temperature as part of the forcing to the surface–troposphere system. This is based on the fact that the time scale of the stratospheric adjustment is a few months, while the surface–atmosphere system needs decades to adjust to the forcing because of the large thermal inertia of the oceans. It is a useful concept in defining the climate sensitivity, the ratio of equilibrium surface–air temperature change and the forcing at the tropopause (Houghton *et al.* 1990). Climate sensitivity is an important input parameter in up–welling diffusion–energy balance climate models, which have been widely used to project future climate changes (e.g., Schlesinger and Jiang 1991; Wigley and Raper 1992).

In this chapter, we present the instantaneous radiative forcing of the Pinatubo aerosol calculated by the UIUC 24–layer ST–GCM without atmospheric responses. The adjusted forcing with the stratospheric temperature adjustment is also estimated using a 1–D column radiative–convective model.

2. Instantaneous Radiative Forcing

The forcing calculations were performed once per hour during a control climate simulation by the 24–layer ST–GCM with prescribed climatological sea–surface temperature and sea–ice distributions (Appendix A). Each hour immediately after the control simulation the radiative–transfer module (RTM) of the GCM was run one more time with the Pinatubo aerosol presented. The presence of the aerosol in the RTM calculation did not influence the control climate simulated by the GCM. The calculation covered the time period from June 1991 through May 1993. For each of the 46 latitudes, 24 layers and 20 spectral bands of the RTM, monthly mean values of the zonal–mean extinction coefficient, single–scattering albedo and asymmetry factor for the Pinatubo volcanic aerosol (Section B) were prescribed at each of the RTM's 72 longitudes. These monthly mean optical properties were kept unchanged during the once–per–hour forcing calculation within each month. Monthly mean net radiative fluxes were obtained by averaging the hourly model

output for each month. The net radiative flux is defined as $N = S - R$, where S is the net incoming solar radiation, defined as positive downward, and R is the net outgoing longwave radiation, defined as positive upward. Then the difference of the net radiative fluxes at each of the 24 layers of the model, $\Delta N = \Delta S - \Delta R$, calculated with and without the aerosol, was derived. Here we focus on the differences at the model top (1 hPa), the tropopause and the earth's surface. The tropopause is defined as the thirteenth sigma layer (~ 200 hPa) (Appendix A) of the ST–GCM.

Fig. 3.5 presents the global–mean radiative forcing from June 1991 to May 1993 at the model top, the tropopause and the earth's surface. The calculated maximum forcing occurs in DJF 1991–1992. It is about –4.9 W/m^2 at the earth's surface, –4.8 W/m^2 at the model top, and –5.7 W/m^2 at the tropopause.

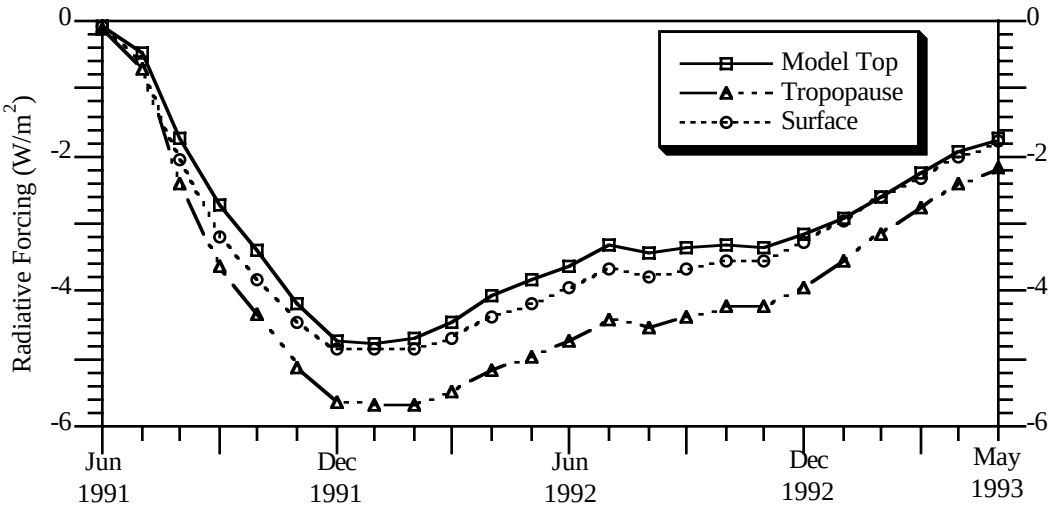

Fig. 3.5 *Global–mean radiative forcing of the 1991 Pinatubo eruption at the model top (1 hPa), the tropopause and the earth's surface calculated by the UIUC 24–layer ST–GCM without atmospheric responses.*

We analyze further the relative importance of different spectral bands to the calculated total forcing, the influence of clouds and the latitudinal distributions of the forcing. Fig. 3.6 presents the latitude–time distributions of zonal–mean radiative forcing at the earth's surface for the solar UV and visible bands (0.175 μm ~ 0.7 μm), solar near–IR bands (0.7 μm ~ 10 μm), all longwave bands, and the total (solar plus longwave) under clear–sky and cloudy–sky conditions, respectively. Figs.

3.7 and 3.8 are the same as Fig. 3.6 except for the radiative forcing at the tropopause and at the top of the model (1 hPa).

First, by analyzing the distributions of total radiative forcing in the three figures we can see that the calculated radiative forcing by the Pinatubo volcanic aerosol is everywhere negative. Overall, the radiative forcing was confined within the tropics and subtropics until August 1991 when there was a southward expansion to the southern–hemisphere high latitudes. A maximum was reached near 60°S in January 1992, which was about a month later than the occurrence of the equatorial maximum. A similar, but weaker, vernal poleward expansion occurred in the Northern Hemisphere in both 1992 and 1993, and again in the Southern Hemisphere in 1992, with associated autumnal retreats. These waxings and wanings of the radiative forcing in the high latitudes of both hemispheres are the result of the meridional transport of aerosol particles and the seasonal variation of solar radiation at a given location. For both clear–sky and cloudy–sky conditions, the negative net radiative forcing is the largest at the tropopause and the smallest at the top of the model. Since clouds scatter solar radiation and absorb longwave radiation, the negative net radiative forcing over the cloudy sky is smaller than over the clear sky. The differences are about 4 W/m^2 for the tropical maximum forcing and 2 to 4 W/m^2 for the maximum forcing in high latitudes.

Second, by comparing the forcing distributions in different spectral bands we can see that the solar forcing is everywhere negative and the longwave forcing is positive. Averaged over all latitudes, the near–IR bands contribute about 50% to the total solar forcing at the top of the model and at the tropopause, and about 40% at the surface. The smaller contribution of the near–IR bands at the surface occurs because of the absorption of the near–IR radiation by tropospheric water vapor

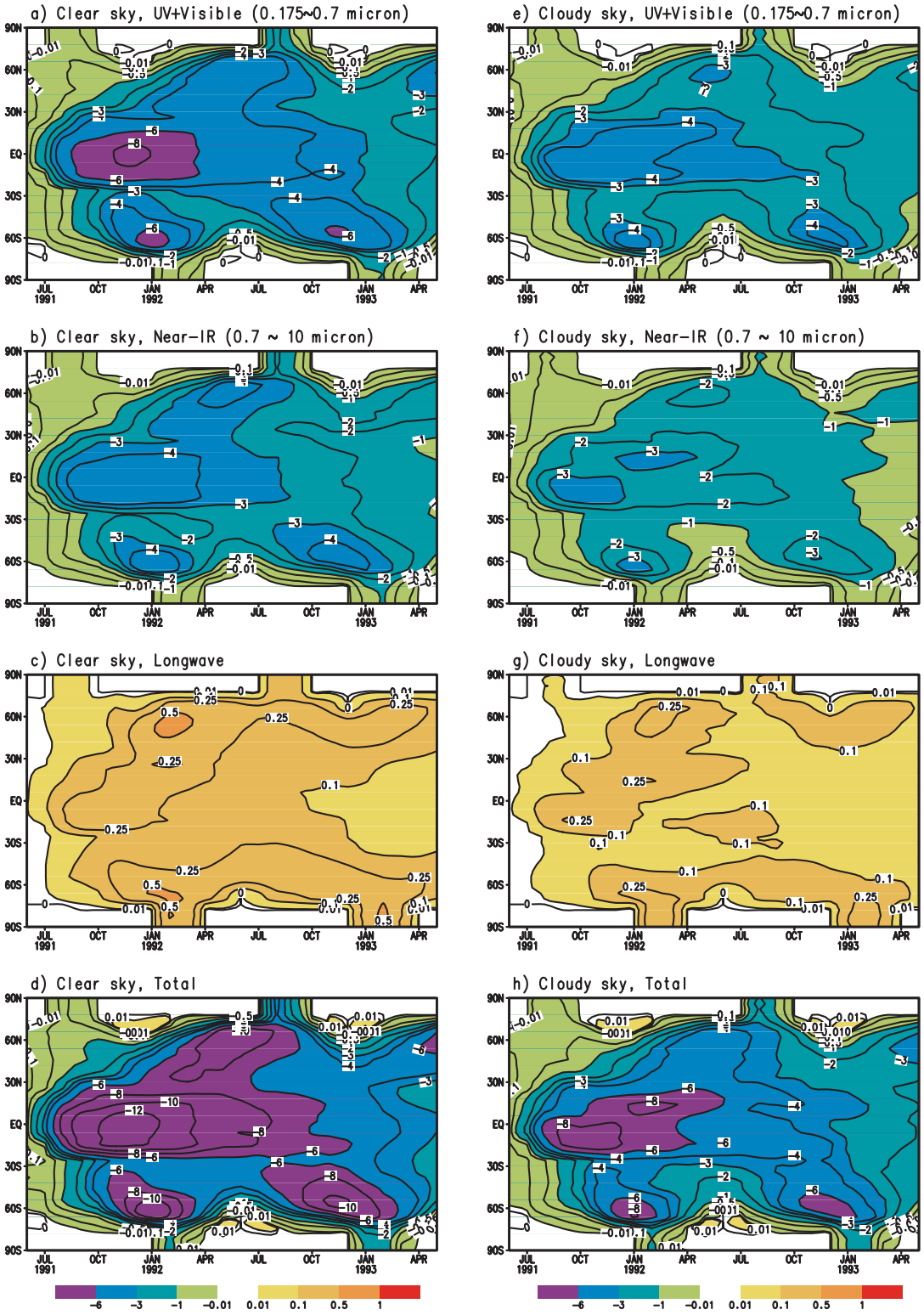

Fig. 3.6. *Latitude–time distributions of zonal–mean radiative forcing (W/m^2) at the earth's surface under clear sky (left panels) and cloudy sky (right panels), respectively. (a) and (e): solar UV and visible bands (0.175 μm ~ 0.7 μm); (b) and (f): solar near–IR bands (0.7 μm ~ 10 μm); (c) and (g): all longwave bands; (d) and (h): the total (solar + longwave).*

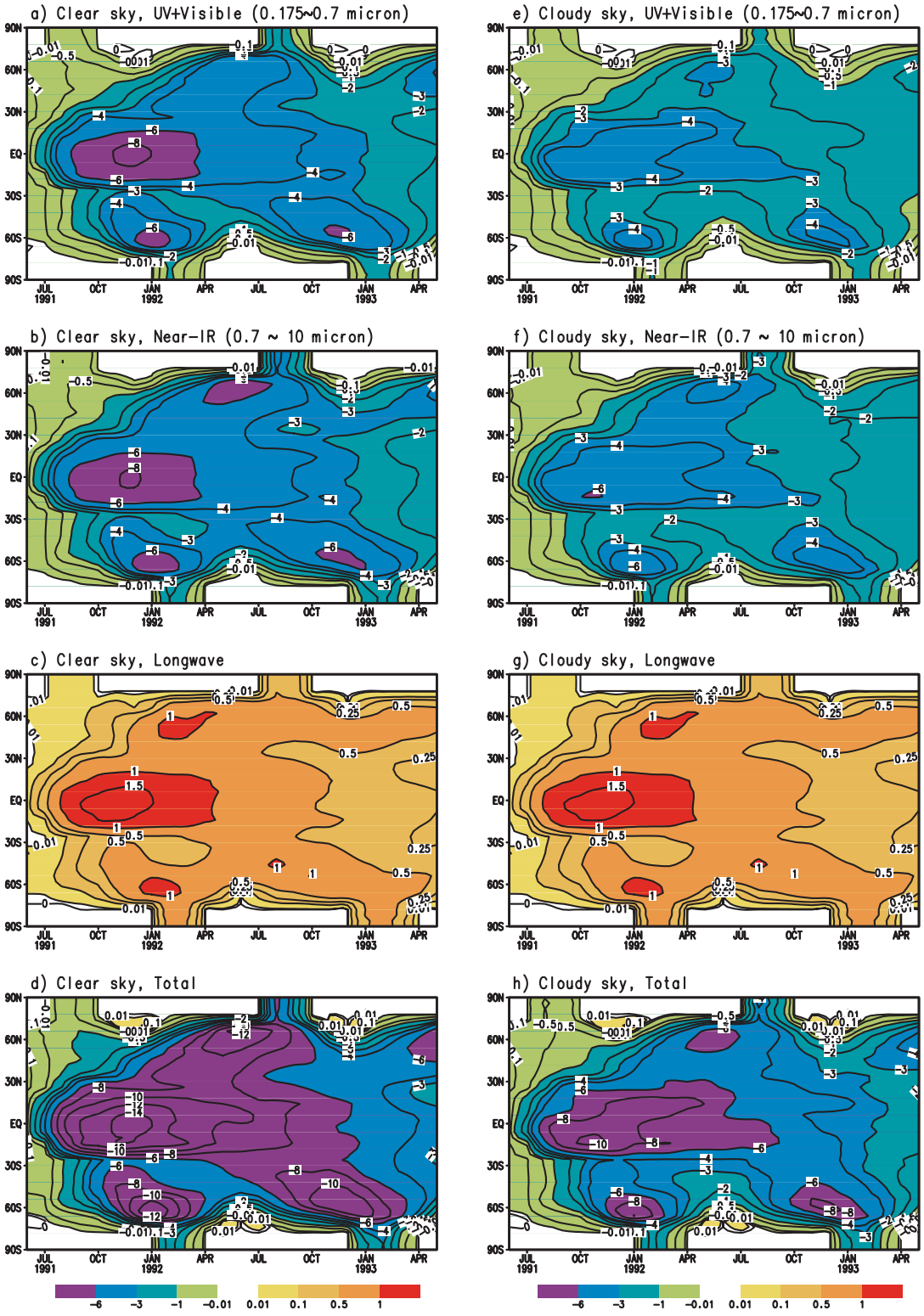

Fig. 3.7. *As in Fig. 3.6, except for the radiative forcing at the tropopause.*

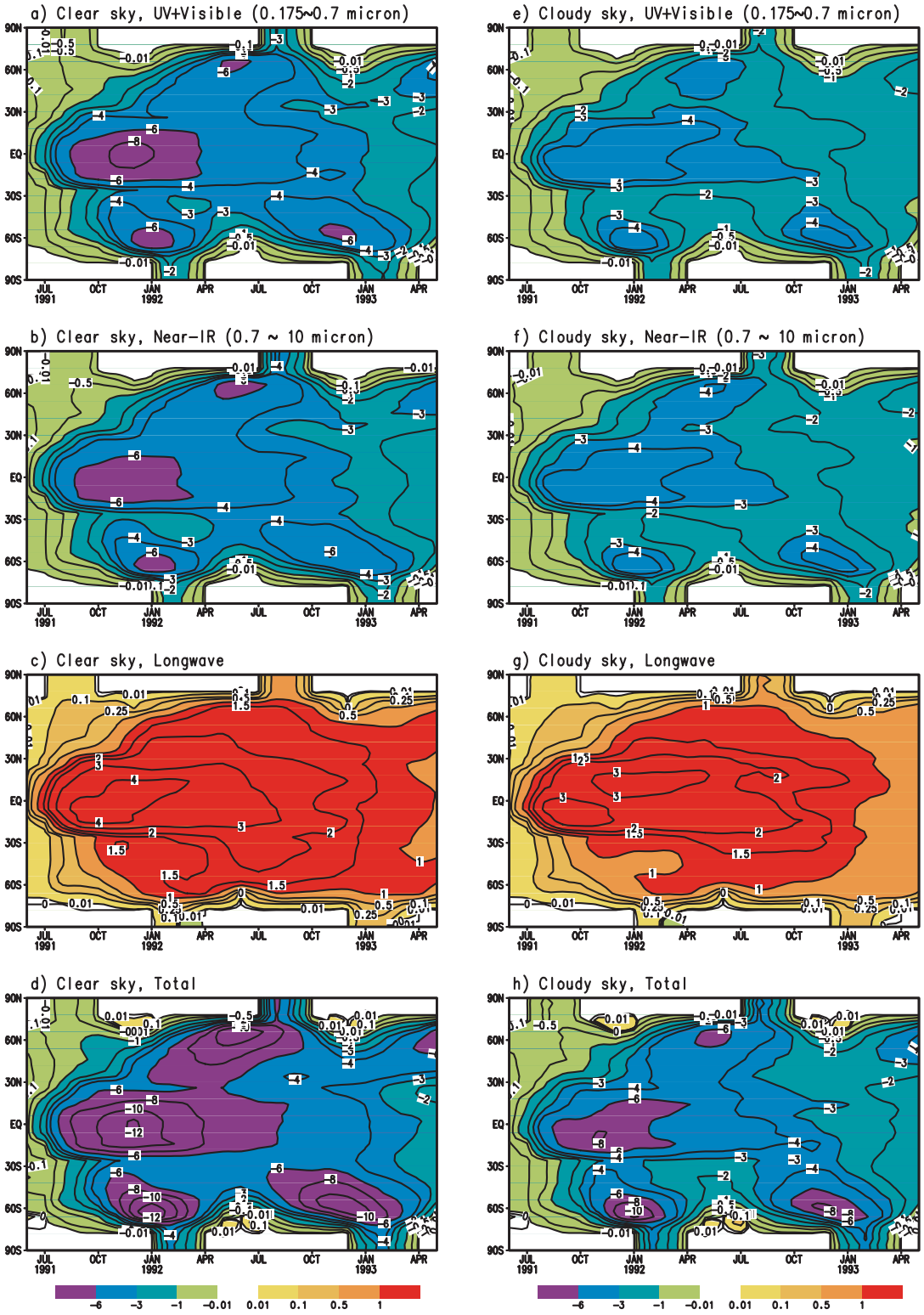

Fig. 3.8. *As in Fig. 3.6, except for the radiative forcing at the model top (1hPa).*

and clouds. The reductions of radiative forcing due to clouds for solar radiation in the UV and visible bands and in the near–IR bands are each about 2 to 4 W/m^2 for the maximum centers at all three levels. Over both clear sky and cloudy sky, the longwave forcing at 1 hPa is an order of magnitude larger than at the surface. This occurs for two reasons. First, the absorption of upward longwave radiation by aerosols in the stratosphere significantly reduces the outgoing longwave radiation at the top of the model. Second, the absorption of downward longwave radiation by water vapor, trace gases and clouds in the troposphere reduces the forcing at the surface, which would otherwise be larger as a result of the emission of longwave radiation by the stratosphere volcanic aerosol.

ST98 calculated the radiative forcing of the Pinatubo eruption using the ECHAM4 GCM. They tested the sensitivity of the forcing to different atmospheric conditions simulated by the ECHAM4 GCM with climatological and real–time SSTs. They found that the forcing was insensitive to the atmospheric conditions. The forcing calculated here by the UIUC 24–layer ST–GCM with fixed climotological SST agrees with ST98's instantaneous forcing in general in its latitudinal distribution and time evolution, but differs in magnitude. The maximum forcing over the tropics is about 3 W/m^2 larger than ST98's. The reasons for this difference are:

1) As described in Section B, following the procedure of ST98 we recalculated the aerosol optical properties for the spatial grid and spectral bands of the UIUC 24–layer ST–GCM. However, we improved the procedure such that the calculated optical depth at 1.02 μm is exactly the same as that observed by SAGE–II. This causes an increase of the optical depth in the visible region compared to that calculated by ST98. Our calculation is closer to the AVHRR observation in the visible region.

2) The UIUC 24–layer ST–GCM extends up to 1 hPa. The ECHAM4 GCM has a lower vertical resolution in the stratosphere, with only one layer between 20 hPa and 0 hPa. When preparing the data of the optical properties for our forcing calculation, we found that the Pinatubo aerosol cloud extended above 10 hPa. For example, from August 1991 to March 1992 the largest extinction efficiency in the visible band (0.4~0.7 μm) was located at 10 hPa, with large values

extending up to 5 hPa in the tropics. This portion of the aerosol optical depth is not well represented by the ECHAM4 GCM.

3) The UIUC ST–GCM has a higher spectral resolution and covers a wider spectral range for both the solar radiation and longwave radiation than does the ECHAM4 GCM. The ECHAM4 GCM has two spectral intervals in the solar, one in the visible (0.25 ~ 0.68 μm) and one in the near–IR (0.68 ~ 4 μm), and 7 basic intervals in the longwave ranging from 3.56 μm to 250 μm. The UIUC ST–GCM has 11 bands in the solar, 8 bands for the UV and visible that range from 0.175 μm to 0.7 μm, 3 bands in the near–IR that range from 0.7 μm to 10 μm, and 9 bands in the longwave that range from 3.33 μm to infinity. This finer spectral resolution may have partially contributed to the larger forcing we obtained.

4) The differences in the simulated geographical distributions of cloud, planetary albedo and temperature between the UIUC ST–GCM and ECHAM4 GCM may have influenced the radiative–forcing calculation. Other factors may have also contributed to the differences in the calculated radiative forcing. For instance, the two models use different timestep for computing the solar radiation – one hour for the UIUC 24–layer ST–GCM and 2 hours for the ECHAM4 GCM.

3. Changes in Radiative Heating and Cooling Rates

To illustrate the impact of Pinatubo volcanic aerosol on the radiative heating of the atmosphere, we present in Fig. 3.9 the latitude–height distributions of the changes of monthly zonal–mean radiative heating rates for the cloudy sky for August 1991 and January 1992. Heating rates for the solar UV and visible bands, the solar near–IR bands and the terrestrial longwave bands are shown separately. The total heating rates over all the bands are also presented. Fig. 3.10 is the same as Fig. 3.9, except for August 1992 and April 1993. The early–time poleward expansion and the later–time decay of the Pinatubo volcanic aerosol in both hemispheres can be seen. Overall, the Pinatubo volcanic aerosol radiatively cooled the troposphere and radiatively warmed the stratosphere. In January 1992, when the radiative forcing reached its maximum, the maximum cooling was about –0.01 °C/day near the surface in the tropics, and the maximum warming was

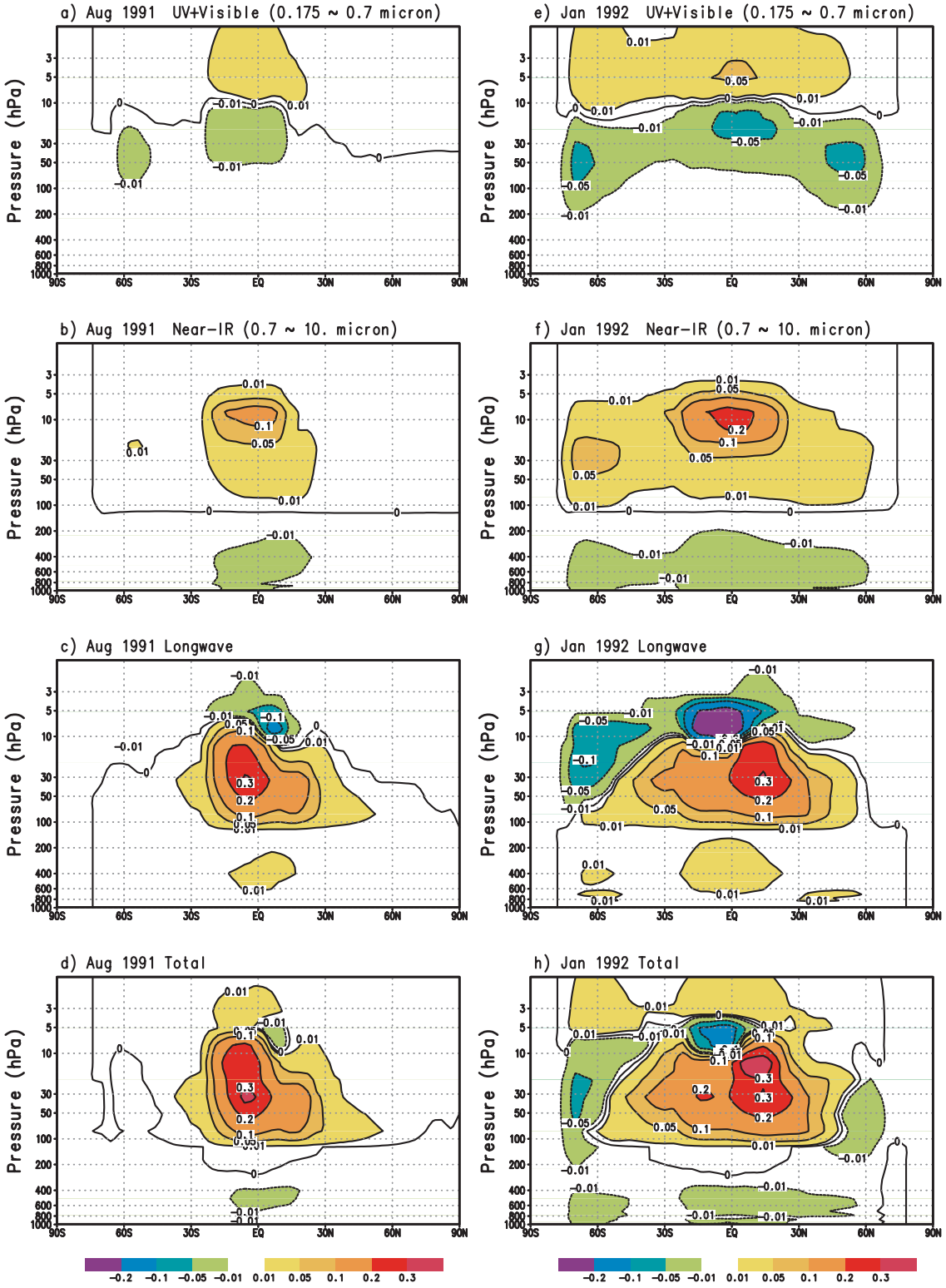

Fig. 3.9. *Latitude–height distributions of the changes of monthly mean zonal–mean radiative heating rates for the cloudy sky for August 1991 (left panels) and January 1992 (right panels). (a) and (e): solar UV and visible bands; (b) and (f): solar near–IR bands; (c) and (g): terrestrial longwave bands; (d) and (h): all bands (solar + longwave).*

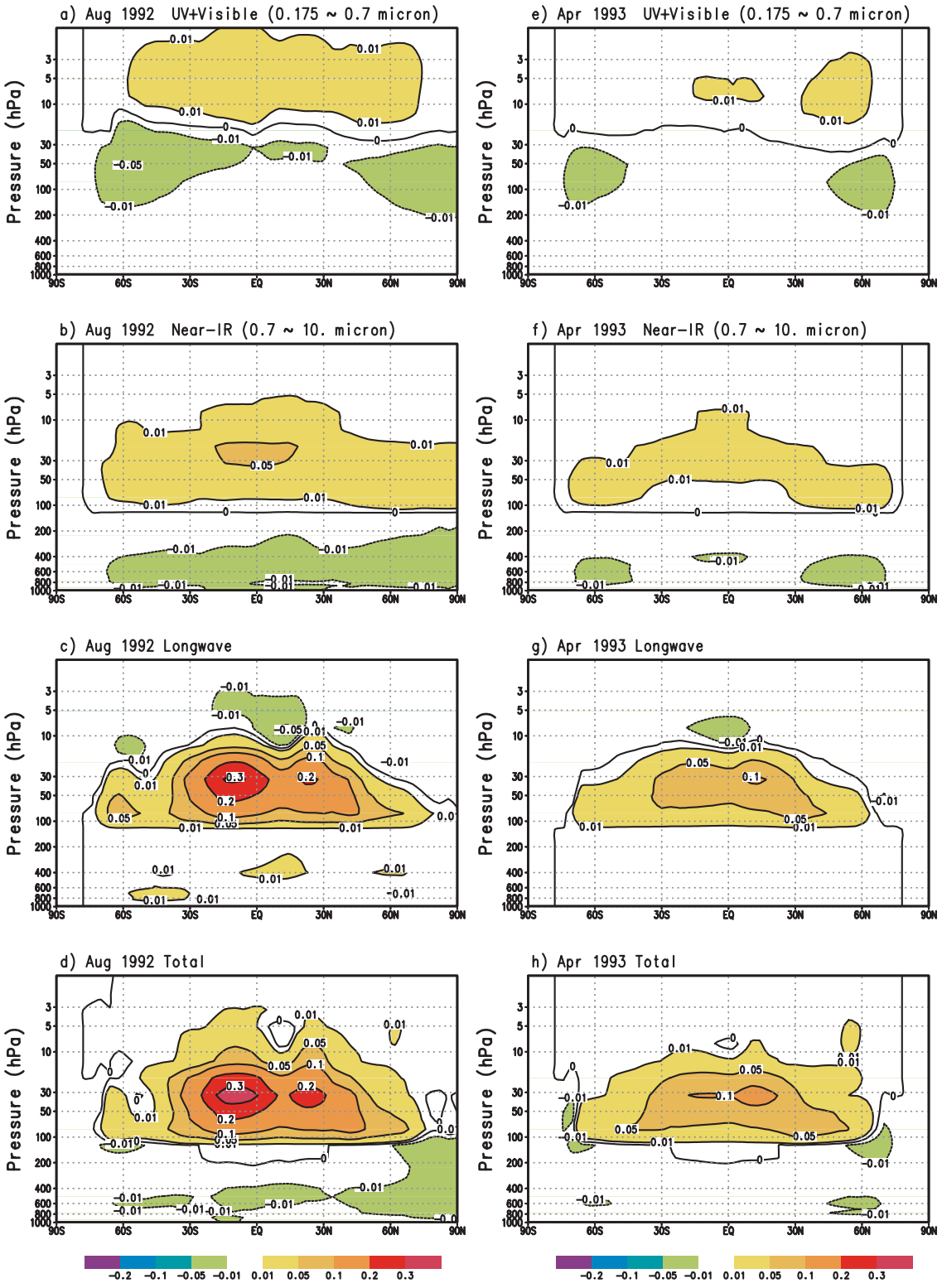

Fig. 3.10. *As in Fig. 3.9, except for August 1992 (left panels) and April 1993 (right panels).*

about 0.3°C/day near 30 hPa in the tropics. Until August 1992, the heating rate was still as large as 0.3°C/day near 30 hPa in the tropics, mainly due to the absorption of longwave radiation by the

aerosol cloud. For each spectral band, the contribution to the atmospheric heating differs. For the longwave radiation, the absorption of upward terrestrial radiation by the aerosol cloud radiatively warmed the lower stratosphere but cooled the upper stratosphere above the aerosol layer. In the troposphere, the downward longwave radiation became larger because of the emission by the aerosol cloud in the stratosphere. The absorption of the enhanced downward longwave radiation by clouds, carbon dioxide and water vapor caused minor warming. For the UV and visible radiation, the back–scattering of the direct incoming solar radiation caused radiative cooling in the atmosphere below the top of the aerosol layer, while the absorption of enhanced up–welling UV and visible radiation by ozone in the upper stratosphere above the aerosol layer caused minor radiative warming. For the near–IR radiation, the back–scattering of incoming solar radiation radiatively cooled the troposphere, most strongly near the surface. But the absorption of near–IR radiation by the aerosol cloud significantly radiatively warmed the stratosphere. This contributed about 30% of the total heating in the middle stratosphere.

ST98 also calculated the changes in radiative heating and cooling rates induced by the Pinatubo aerosol using the ECHAM4 GCM. In comparison with Fig. 10 of ST98, the maximum changes in the UV and visible band and the near–infrared band calculated here closely match those of ST98 in magnitude, time and location. This indicates that the calculation of solar heating rate anomalies is robust in spite of the many differences between these two studies, such as the different vertical resolutions between the UIUC 24-layer ST–GCM and the ECHAM4 GCM. The changes in longwave heating rates calculated here are about 0.05 to 0.1 ℃ larger for the maxima than those of ST98. The centers of longwave heating anomalies extend up to 10 hPa in the tropics in Figs. 3.9 and 3.10, and extend only up to 30 hPa in Fig.10 of ST98. Kinnison *et al.* (1994) also calculated the changes in heating rate and cooling rates induced by the Pinatubo aerosol for October 1991. Near the equator, the maximum longwave heating anomaly is 0.27 ℃/day at about 25 km and the maximum total solar heating anomaly is 0.33 ℃/day at about 30 km. Since Kinnison *et al.* (1994) used a single–scattering albedo of 0.9 for all solar bands to roughly account for a carbon aerosol component, their solar heating anomaly is slightly larger than what we have at the equator in October 1991 (pictures not shown). The longwave heating rate anomaly calculated by Kinnison *et al.*

(1994) is close to the present study. It should be pointed out that these comparisons are qualitatively because of the differences in aerosol data and model structures. However, the heating rate anomalies from the three studies are rather close to each other.

4. Adjusted Radiative Forcing

Volcanic aerosols radiatively warm the stratosphere because of the absorption of near–IR radiation and terrestrial longwave radiation by the aerosol clouds. By allowing the stratospheric temperature to adjust, but fixing the temperature of the surface–troposphere system, the outgoing longwave radiation at the model top and the downward longwave radiation at the tropopause will increase as a result of the higher emitting temperature of the stratosphere. The adjustment continues until there is no flux divergence of radiation in the stratosphere. Consequently, the vertical distribution of calculated radiative forcing changes.

Technically it is difficult to estimate the adjusted radiative forcing by using a GCM. The GCM has to be run with fixed surface–troposphere temperature but with changing stratospheric temperature until the stratosphere reaches radiative equilibrium. For the Pinatubo volcanic eruption, since the aerosol distribution changed month by month, such equilibrium integration must be performed for each month. We simplify the procedure by running a 1–D radiative–convective model (RCM), which resembles the RCM of Schlesinger *et al.* (1997). This RCM has 24 layers in σ–coordinate, with σ values set to be the same as those of the 24–layer ST–GCM (Appendix A). The RCM uses the radiation routines of the 24–layer ST–GCM.

The instantaneous net radiative forcing calculated at the tropopause consists of the shortwave forcing, ΔS, which is almost the same as the shortwave forcing at the model top (compare Fig. 3.7 with Fig. 3.8), and the longwave forcing, $-\Delta R$, which is much smaller at the tropopause than at the model top. The adjustment of the net radiative forcing occurs only in the longwave, and the value of the adjusted longwave radiative forcing at the tropopause, ΔR_{adj}^{TR}, lies between the instantaneous longwave forcings at the model top, ΔR^{top}, and at the tropopause, ΔR^{TR}. Accordingly we express ΔR_{adj}^{TR} as

$$\Delta R_{adj}^{TR} = \alpha \Delta R^{top} + (1-\alpha)\Delta R^{TR} \quad \text{or} \quad \Delta R_{adj}^{TR} - \Delta R^{TR} = \alpha\left(\Delta R^{top} - \Delta R^{TR}\right)$$

with the interpolation factor α being in the range of (0, 1). This allows us to estimate α by regression using the instantaneous and adjusted longwave forcing calculated by the 1–D RCM for different aerosol profiles in the stratosphere under different climatic conditions.

For the 1–D RCM calculation, selected atmospheric vertical profiles (pressure, temperature, water vapor, cloud water/ice, cloudiness and ozone) and surface albedo, ground temperature, solar constant and solar zenith angle, were taken from the 15th year of the 24–layer ST–GCM control simulation (Appendix A). To cover a wide range of climatic conditions and geographical locations we chose profiles in January, April, July and October for latitudes between 74°S and 74°N with an 8° interval, and longitudes between 0° and 360° with a 25° interval. The volcanic aerosol is located between the 11th and 5th σ–layers of the model atmosphere, which correspond to 100 hPa and 5 hPa for a surface pressure of 1000 hPa, with a maximum mass mixing ratio of $7\text{x}10^{-8}$ g(SO_4^{-2})/g at about 9 hPa. This distribution resembles the Pinatubo volcanic aerosol in the tropics before February 1993 (see Fig. 3.4). All together we performed calculations for 349 different cases. For all cases, identical aerosol optical properties were used. They were calculated using a Mie theory model (Appendix B). The broadband aerosol optical properties are presented in tables in Appendices A and B.

For each case, we first ran the 1–D RCM to equilibrium without volcanic aerosol. Then we added volcanic aerosol and ran the model to a new equilibrium with the ground and tropospheric temperatures fixed, and the stratospheric temperatures free to adjust radiatively. The resulting distribution of $\Delta R_{adj}^{TR} - \Delta R^{TR}$ against $\Delta R^{top} - \Delta R^{TR}$ and the fit are presented in Fig. 3.11. The distribution is linear as expected with the fitting coefficient α = 0.39 and correlation coefficient R=0.95. We have run a few more sets of experiments using the 1–D RCM with different vertical distributions of aerosol in the stratosphere and obtained almost the same α with errors less than 10%. Applying the linear empirical function in Fig. 3.11 to the instantaneous longwave forcings of the Pinatubo aerosol at all model grids calculated by using the 3–D RCM of the UIUC 24–layer ST–GCM in Section C.2, we obtained the geographical distributions of the adjusted longwave forcing at the tropopause for the Pinatubo eruption.

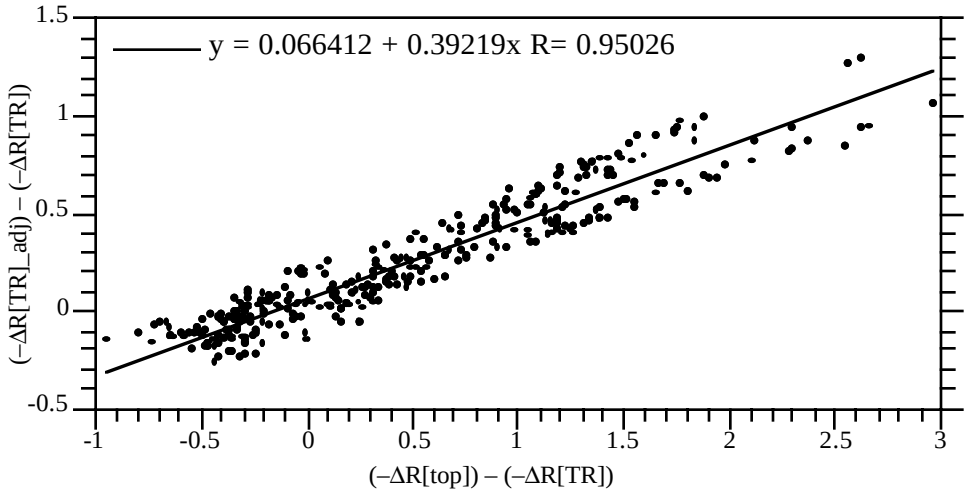

Fig. 3.11. *Scatter distributions of* $\Delta R^{TR}_{adj} - \Delta R^{TR}$ *against* $\Delta R^{top} - \Delta R^{TR}$ *and the linear fit.*

Fig. 3.12 presents the latitude–time distributions of the zonally averaged adjusted longwave forcing and the adjusted net forcing over cloudy sky. Comparing the adjusted forcing in Fig. 3.12 to the instantaneous forcing in Fig. 3.7, one can see that the maximum longwave forcing in the tropics increased by 0.5 to 1.0 W/m^2 with the stratospheric adjustment. The maximum negative net forcing in the tropics is –8 W/m^2 after the adjustment, and –10 W/m^2 before the adjustment. The global–mean instantaneous and adjusted longwave and net radiative forcings at the tropopause over cloudy sky are presented in Fig. 3.13. Though the percent change of longwave forcing is about 60%, the change in net radiative forcing is less than 10% because of the relative small contribution of the instantaneous longwave forcing to the instantaneous net forcing. The adjusted maximum global–mean net radiative forcing is –5.3 W/m^2 in January 1992.

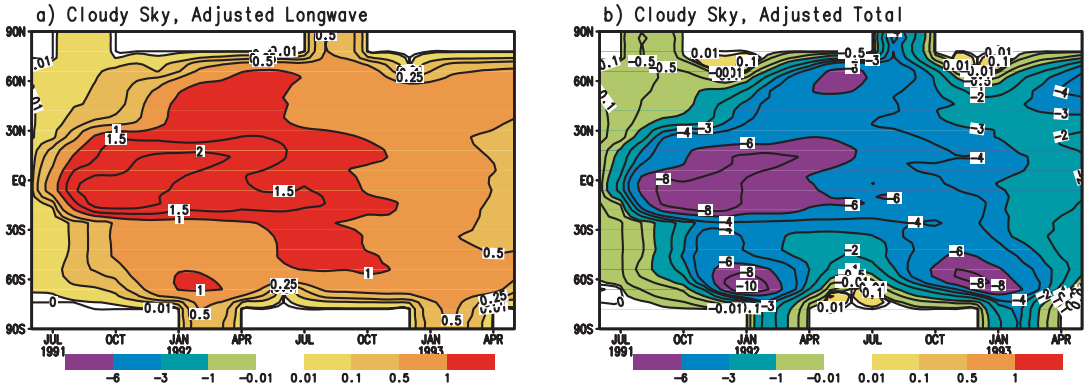

Fig. 3.12. *Adjusted (a) longwave and (b) net radiative forcing at the tropopause over cloudy sky.*

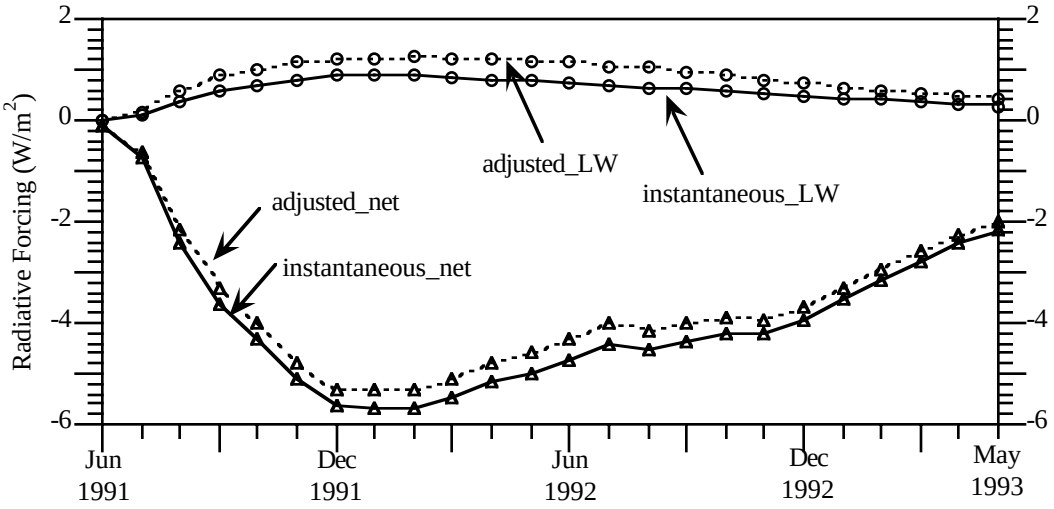

Fig. 3.13. *Instantaneous and adjusted global–mean longwave and net radiative forcings at the tropopause over cloudy sky.*

D. Summary

In this chapter we compared first the optical properties of the Pinatubo volcanic aerosol from different sources. The optical properties reconstructed for the UIUC ST–GCM supercede those in Stenchikov *et al.* (1998) reconstructed for the ECHAM4 GCM. The column–integrated optical depth at 0.55 μm reconstructed for the UIUC ST–GCM lies between the SAGE–II and AVHRR satellite observations. The maximum global–mean optical depth at 0.55 μm for the UIUC reconstruction is about 0.23 in early 1992.

Then, we calculated the radiative forcing of the Pinatubo volcanic aerosol for the two years following the eruption using the UIUC 24–layer ST–GCM. Solar forcing is everywhere negative and the longwave forcing is positive. Averaged over all latitudes, the near–IR bands contribute about 50% to the total solar forcing at the top of the model and at the tropopause and about 40% at the surface. The longwave forcing at 1 hPa is an order of magnitude larger than that at the surface. The calculated maximum global–mean net radiative forcing occurs in DJF 1991–1992. It is about –4.9 W/m^2 at the surface, –4.8 W/m^2 at the model top, and –5.7 W/m^2 at the tropopause. Overall, the radiative forcing was confined within the tropics and subtropics, with secondary maxima in high latitudes. The forcing over cloudy sky is smaller than that over clear sky. The differences are about 4 W/m^2 for the tropical maxima and 2 to 4 W/m^2 for the maxima in high latitudes. Our results are generally larger than those of ST98.

Heating–rate calculations showed that overall the Pinatubo volcanic aerosol radiatively cooled the troposphere and radiatively warmed the stratosphere. The calculated maximum cooling rate is about –0.01°C/day near the surface in the tropics and the maximum warming rate is about 0.3°C/day near 30 hPa in the tropics in January 1992. The absorption of upward terrestrial radiation by the aerosol cloud warmed the lower stratosphere but cooled the upper stratosphere above the aerosol layer. The back–scattering of the direct incoming solar radiation in the UV and visible regions radiatively cooled the atmosphere below the top of the aerosol layer, while the absorption of the enhanced up–welling UV and visible radiation by ozone in the upper stratosphere above the aerosol layer caused minor warming. For the near IR, the back–scattering of incoming solar radiation radiatively cooled the troposphere. But the absorption of the near–IR radiation by the

aerosol cloud radiatively warmed the stratosphere. This contributed about 30% of the total heating in the middle stratosphere.

Finally, we estimated the forcing with the stratospheric temperature adjustment using a 1–D radiative–convective model. At the tropopause, after adjustment, the maximum longwave forcing in the tropics increased by 0.5 to 1.0 W/m^2. The adjusted maximum net forcing in the tropics is –8 W/m^2. The adjusted global–mean forcing is about 10% smaller than the instantaneous global–mean forcing. The adjusted maximum global–mean net radiative forcing is –5.3 W/m^2 in DJF 1991–1992.